PHYSICAL REVIEW D **106,** 084030 (2022)

Multidomain spectral code for punctures without excision: The spherical case

H. P. de Oliveira*

Departamento de Física Teórica—Instituto de Física A. D. Tavares,
Universidade do Estado do Rio de Janeiro, R. São Francisco Xavier, 524, Rio de Janeiro, RJ, 20550-013,
Brazil and Department of Physics and Astronomy, Bowdoin College, Brunswick, Maine 04011, USA

(Received 11 August 2022; accepted 4 October 2022; published 19 October 2022)

We present the first spectral method to evolve a single black hole treated as a puncture, therefore without singularity excision. We consider the Galerkin-Collocation method in single and multidomains to integrate the extended Baumgarte-Shapiro-Shibata-Nakamura formulation. In addition, we adopt the moving puncture approach but consider distinct Bona-Massó slicing families instead of the standard $1 + \log$ slicing condition. Further, we implement the maximal slicing version of the spectral code, where the lapse satisfies an elliptic-like equation.

DOI: 10.1103/PhysRevD.106.084030

I. INTRODUCTION

Recasting the original ADM equations or $3 + 1$ formulation of the Einstein equations to strongly hyperbolic formulations was one of the main factors of successful binary black hole simulations [1–3]. Henceforth, the Baumgarte-Shapiro-Shibata-Nakamura (BSSN) [4–6] formulation, together with some of its variations, constitutes the backbone of current numerical relativity works. Another crucial ingredient was the use of the moving puncture approach that consisted of the $1 + \log$ slicing [7] and the gamma-driver conditions [8,9]. Brown [10] extended the original BSSN formulation suited for Cartesian coordinates to include any curvilinear coordinate system. In particular, the new recast set of equations is more suited to describe many astrophysical problems where spherical or cylindrical coordinates, for instance, adapt better.

The idea of representing a black hole as a puncture without the need to excise its inner region or to impose an isometry condition at the throat is structurally simple and elegant [11]. To deal numerically with the inherent singularity at the black hole center, one has to guarantee that no grid points coincide with this locus. This strategy started by considering fixed punctures [9] but later evolved into the moving puncture, which plenty of numerical works nowadays adopt.

Spectral methods have become a viable and attractive technique for numerical relativity problems [12]. The primary feature of any spectral method is to express the approximate solution as a series expansion in a set of basis functions such as Chebyshev, Legendre, or Fourier functions. For smooth problems, the spectral methods converge exponentially to the exact solution when we increase the resolution or the number of terms in the series expansion.

By focusing on spacetimes containing black holes, the determination of the initial data with one or more black holes represented the first application of spectral methods in numerical relativity [13–19]. Most works on the simulations involving a single black hole [20–22] or a black hole binary system [23,24] (see also the references therein) with spectral methods belong to the Caltech/Cornell group that deal with the generalized harmonic formulation of the field equations. Tichy [22] has considered the BSSN equations to evolve a single black hole. The Meudon group [25] also adopted the BSSN equation with spectral methods in the framework of the constrained evolution. In addition, excising the black hole interior to remove the singularity from the spatial or physical domain is another common aspect shared by all mentioned works. In this matter, we mention that the Caltech/Cornell group solved the field equations by introducing the dual coordinate method to excise the black hole interiors in a dynamical setting [26].

In the present work, we propose implementing single and multidomain Galerkin-Collocation (GC) algorithms to evolve a single black hole without excision with the BSSN equations in spherical coordinates. We have considered the moving puncture approach with the Bona-Massó and the gamma-driver conditions to evolve the lapse shift vector. In this instance, we choose distinct Bona-Massó functions [27–30] besides the one corresponding to the standard $1 + \log$ slicing.

We remark that the GC method adopts the basis functions as appropriate combinations of the Chebyshev polynomials to satisfy the boundary conditions identically. Henrichs [31–33] has demonstrated the advantage of such an approach by reducing the roundoff error near the end points. Another distinctive aspect in most applications of

---

[*] henrique.oliveira@uerj.br

the GC method is the use of suitable mappings to compactify the semi-infinite spatial domain into a finite computational domain [34] [e.g., Eq. (29)]. See Refs. [35–38] for some previous works on the GC method in different problems.

We have organized the paper as follows: We outline the equations of the extended or generalized BSSN formulation for spherically symmetric spacetimes in Sec. II. We describe in Sec. III the basic scheme of the single and multidomain numerical implementations of the GC method without excision. Section IV presents the numerical tests that verify the analytical solutions of the Schwarzschild black hole in different foliations or geometries, the transition from the wormhole to trumpet foliations, and the power-law behavior of the lapse near the puncture. In these experiments, we have considered other Bona-Massó families besides the standard $1 + \log$ slicing. In Sec. V, we summarize the results and indicate possible directions of the present research.

II. THE BSSN FORMULATION IN SPHERICAL SYMMETRY

A. Basic definitions

We follow closely Refs. [39–41] to establish the field equations in the BSSN formulation using spherical coordinates introduced by Brown [10]. The line element for spherically symmetric spacetimes is written as

$$ds^2 = -(\alpha^2 - \beta_r\beta^r)dt^2 + 2\beta_r dr dt + \mathrm{e}^{4\phi} d\bar{l}^2, \tag{1}$$

where $\alpha(t,r)$ is the lapse, $\beta^i = (\beta^r, 0, 0)$ is the shift vector with $\beta^r = \beta^r(t,r)$, and $\phi(t,r)$ is the BSSN conformal factor. The conformally related spatial line element $d\bar{l}^2$ is

$$d\bar{l}^2 = \bar{\gamma}_{ij} dx^i dx^j = a(t,r)dr^2 + r^2 b(t,r)(d\theta^2 + \sin^2\theta d\varphi^2), \tag{2}$$

where $a(t,r)$ and $b = b(t,r)$ are the metric functions.

Unlike the original BSSN formulation, the background metric denoted by $\hat{\gamma}_{ij}$ is written in spherical coordinates instead of Cartesian coordinates. To fix the present notation, we have

$$\hat{\gamma}_{ij} = \mathrm{diag}(1, r^2, r^2 \sin^2\theta). \tag{3}$$

From Eq. (1), the relation between the physical and the conformal metric is

$$\bar{\gamma}_{ij} = \mathrm{e}^{4\phi}\gamma_{ij}, \tag{4}$$

and consequently, it follows that

$$\mathrm{e}^{4\phi} = \left(\frac{\gamma}{\bar{\gamma}}\right)^{1/3}. \tag{5}$$

We fix initially $\bar{\gamma}(t=0) = \hat{\gamma}$ [10], where $\hat{\gamma}$ is the determinant of the background metric. In addition, we have adopted the so-called Brown's "Lagrangian" condition

$$\partial_t \bar{\gamma} = 0. \tag{6}$$

We complete the presentation of the relevant quantities that appear in the field equations with the traceless part of the conformal extrinsic curvature

$$\bar{A}_{ij} = \bar{K}_{ij} - \frac{1}{3}\bar{\gamma}_{ij}K, \tag{7}$$

where $K = \gamma^{ij}K_{ij}$ is the trace of the extrinsic curvature, and $\bar{K}_{ij} = \mathrm{e}^{-4\phi}K_{ij}$, with K_{ij} being the physical extrinsic curvature. For spherically symmetric spacetimes, the components of $\bar{A}_{ij}$ are

$$\bar{A}_{ij} = \mathrm{diag}(\bar{A}_{rr}, r^2\bar{A}_{\theta\theta}, r^2\sin^2\theta\bar{A}_{\theta\theta}), \tag{8}$$

with the condition $\bar{\gamma}^{ij}\bar{A}_{ij} = \bar{A}_{rr}/a + 2\bar{A}_{\theta\theta}/b = 0$. Following Ref. [39], we define

$$A_a = \bar{A}^r_r = \frac{\bar{A}_{rr}}{a}, \qquad A_b = \bar{A}^\theta_\theta = \frac{\bar{A}_{\theta\theta}}{b}, \tag{9}$$

which yields

$$A_a + 2A_b = 0. \tag{10}$$

The last independent variable is the connection vector $\bar{\Delta}^i$ defined by

$$\bar{\Delta}^i = \bar{\gamma}^{jk}\Delta\Gamma^i_{jk} = \bar{\gamma}^{jk}(\bar{\Gamma}^i_{jk} - \hat{\Gamma}^i_{jk}), \tag{11}$$

where $\bar{\Gamma}^i_{jk}$ and $\hat{\Gamma}^i_{jk}$ are the connections associated with the conformal and the background metrics, respectively. For spherically symmetric spacetimes, the connection vector has only one component,

$$\bar{\Delta}^i = (\bar{\Delta}^r, 0, 0), \tag{12}$$

with

$$\bar{\Delta}^r = \frac{1}{a}\left[\frac{\partial_r a}{2a} - \frac{\partial_r b}{b} - \frac{2}{r}\left(1 - \frac{a}{b}\right)\right]. \tag{13}$$

B. Evolution equations

We now display the evolution equations for all relevant variables, which are, in the present case, the metric functions $a(t,r)$ and $b(t,r)$, the conformal factor $\phi(t,r)$, the component $A_a(t,r)$ [note that $A_b(t,r) = -A_a/2$], the trace of the extrinsic curvature $K(t,r)$, and the component $\bar{\Delta}^r(t,r)$ of the connection vector. Since we are focusing on describing black holes as punctures without excision with spectral methods, we will not include matter in the field equations.

The evolution equation for the conformal factor assumes the form [39]

$$\partial_t\phi = \beta^r\partial_r\phi + \bar{\nabla}_k\beta^k - \frac{1}{6}\alpha K, \tag{14}$$

where $\bar{\nabla}_k$ is the covariant derivative with respect to the conformal metric, and as a consequence

$$\bar{\nabla}_k\beta^k = \partial_r\beta^r + \left(\frac{\partial_r a}{2a} + \frac{\partial_r b}{b} + \frac{2}{r}\right)\beta^r. \tag{15}$$

The conformal factor diverges at the puncture location; therefore, it is not a regular function. Thus, to deal with an everywhere well-defined function, we introduce a new quantity $\chi(t,r)$ related to the conformal factor by

$$\chi \equiv \mathrm{e}^{-n\phi}, \tag{16}$$

where n is an integer number. The above relation has been used in Ref. [40] with $n = 2$; in Ref. [2], the choice was $n = 1$, which characterizes the χ method. Combining Eqs. (14) and (16), we obtain the following evolution equation for χ:

$$\partial_t\chi = \beta^r\partial_r\chi - \frac{n}{6}\chi\bar{\nabla}_k\beta^k + \frac{n}{6}\chi\alpha K. \tag{17}$$

The evolution equations for the metric functions a and b are

$$\partial_t a = \beta^r\partial_r a + 2a\partial_r\beta^r - \frac{2}{3}a\bar{\nabla}_k\beta^k - 2\alpha a A_a, \tag{18}$$

$$\partial_t b = \beta^r\partial_r b + 2b\frac{\beta^r}{r} - \frac{2}{3}b\bar{\nabla}_k\beta^k + \alpha a A_a, \tag{19}$$

where we have replaced $A_b = -A_a/2$.

The evolution equation for the trace of the extrinsic curvature is

$$\partial_t K = \beta^r\partial_r K + \frac{1}{3}\alpha K^2 + \frac{3}{2}\alpha A_a^2 - \nabla^2\alpha, \tag{20}$$

where the Laplacian of the lapse is calculated with the physical spatial metric taking into account the redefinition of the conformal factor. Then,

$$\nabla^2\alpha = \frac{\chi^{4/n}}{a}\left[\partial_r^2\alpha - \left(\frac{\partial_r a}{2a} - \frac{\partial_r b}{b} + \frac{2}{n}\frac{\partial_r\chi}{\chi} - \frac{2}{r}\right)\partial_r\alpha\right]. \tag{21}$$

It is possible to implement the maximal slicing evolution by setting $\partial_t K = K = 0$, which results in an elliptic-type equation for the lapse. In the next section, we have explored this possibility with the spectral code.

We proceed with the presentation of the evolution equations for $A_a(t,r)$ and $\bar{\Delta}^r(t,r)$. For the first function, we have

$$\partial_t A_a = \beta^r\partial_r A_a - \left(\nabla^r\nabla_r\alpha - \frac{1}{3}\nabla^2\alpha\right) + \alpha\left(R^r_r - \frac{1}{3}R\right) + \alpha K A_a, \tag{22}$$

where

$$\nabla^r\nabla_r\alpha - \frac{1}{3}\nabla^2\alpha = \frac{\chi^{4/n}}{3a}\left[2\partial_r^2\alpha - \left(\frac{\partial_r a}{a} + \frac{\partial_r b}{b} + \frac{8}{n}\frac{\partial_r\chi}{\chi} + \frac{2}{r}\right)\partial_r\alpha\right]. \tag{23}$$

R^r_r is the mixed radial component of the Ricci tensor associated with the physical metric, and $R = \gamma^{ij}R_{ij}$ is its trace [39].

The last evolution equation is

$$\begin{aligned}\partial_t\bar{\Delta}^r &= \beta^r\partial_r\bar{\Delta}^r - \bar{\Delta}^r\partial_r\beta^r + \frac{1}{a}\partial_r^2\beta^r + \frac{2}{b}\partial_r\left(\frac{\beta^r}{r}\right) \\ &\quad + \frac{2}{3}\bar{\Delta}^r(\bar{\nabla}_k\beta^k) + \frac{1}{3a}\partial_r(\bar{\nabla}_k\beta^k) - \frac{2A_a}{a}\left(\partial_r\alpha + \frac{6\alpha}{n}\frac{\partial_r\chi}{\chi}\right) \\ &\quad + 2\alpha A_a\left[\bar{\Delta}^r + \frac{3}{ar}\left(1 - \frac{a}{b}\right) + \frac{3\partial_r b}{2ab}\right] - \frac{4\alpha}{3a}\partial_r K,\end{aligned} \tag{24}$$

where we have followed the form adopted in Ref. [41] [see Eq. (9e)].

The gauge conditions dictate the evolution of the lapse α and the shift vector β^i. The moving puncture conditions [2,3,9,42] become the standard choices for the numerical evolution of black hole spacetimes. Then, we adopt for the lapse the Bona-Massó condition

$$\partial_t\alpha = \beta^i\partial_i\alpha - \alpha^2 f(\alpha)K, \tag{25}$$

where the choice of the Bona-Massó family $f(\alpha)$ specifies the slicing under consideration. For instance, if $f(\alpha) = 1$, we have the harmonic slicing, whereas $f(\alpha) = 2/\alpha$ characterizes the $1 + \log$ condition. It is possible to choose other families of the Bona-Massó function $f(\alpha)$ that can offer advantages from a numerical perspective [30,43].

We have considered the following form of the gamma-freezing condition for the shift vector:

$$\partial_t \beta^i = \frac{3}{4} B^i, \qquad \partial_t B^i = \partial_t \bar{\Delta}^i - \eta \beta^i. \tag{26}$$

In these equations, we can use variant forms that arise after replacing some or all of the ∂_t derivatives with $\partial_t - \beta^i \partial_i$ [44].

Finally, to complete the set of field equations, we present the Hamiltonian and momentum constraints

$$\mathcal{H} = R - \frac{3}{2} A_a^2 + \frac{2}{3} K^2 = 0 \tag{27}$$

$$\mathcal{M}^r = \partial_r A_a - \frac{2}{3} \partial_r K - \frac{6A_a}{n\chi} \partial_r \chi + \frac{3A_a}{2} \left(\frac{2}{r} + \frac{\partial_r b}{b} \right) = 0. \tag{28}$$

Both equations constitute valuable tests for the code, since they must be satisfied along the dynamics.

III. THE MULTIDOMAIN GALERKIN-COLLOCATION METHOD

We present the numerical procedure based on the Galerkin-Collocation method in multiple nonoverlapping subdomains to integrate the BSSN equations (17)–(20), (22), and (24)–(26). We have followed the procedure outlined in Ref. [35], which allows us to skip some details of the implementation.

The first step is the compactification of the spatial domain using the following map:

$$r = L_0 \frac{(1+x)}{1-x}, \tag{29}$$

where L_0 is the map parameter and $x \in [-1, 1]$ is a computational domain from which we define the collocation points. Other transformations can map semi-infinite intervals into a finite domain, but the above one is more suitable for those problems with functions decaying algebraically with r [34].

Figure 1 shows the basic scheme for implementing the multidomain spectral code. Notice that for a single domain code, we use the mapping (29) defining the computational x, while for introducing multiple subdomains, we add n_d computational subdomains parametrized by $-1 \leq \xi^{(l)} \leq 1$, $l = 1, 2, \ldots, n_d$ corresponding to each subdomain $\mathcal{D}_l$. In more detail, according to Fig. 1, the physical domain $\mathcal{D}: 0 < r < \infty$ is divided into n_d subdomains $\mathcal{D}_1: 0 < r < r^{(1)}, \ldots, \mathcal{D}_l: r^{(l-1)} \leq r \leq r^{(l)}, \ldots, \mathcal{D}_{n_d}: r^{(n_d-1)} \leq r < \infty$, where $r_0 = 0$ (excluded from the physical domain) and $r^{(1)}, r^{(2)}, \ldots, r^{(n_d-1)}$ are the interface between contiguous subdomains. We establish that $x = x(\xi^{(l)})$, $l = 1, 2, \ldots, n_d$ are linear transformations connecting $x^{(l-1)} \leq x \leq x^{(l)}$ into $-1 \leq \xi^{(l)} \leq 1$ (see Ref. [35] for details).

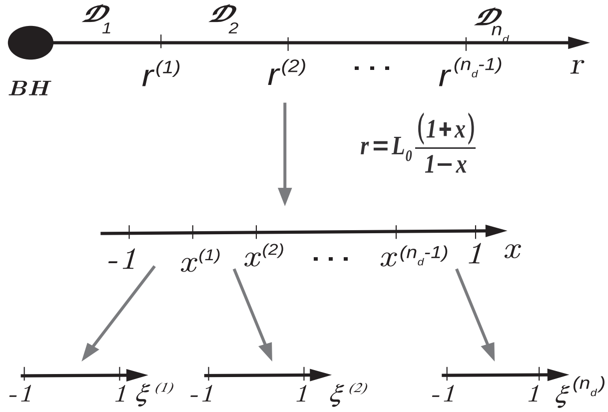

FIG. 1. Basic scheme showing the subdomains $\mathcal{D}_1, \mathcal{D}_2, \ldots, \mathcal{D}_{n_d}$ covered by the computational subdomains $-1 \leq \xi^{(j)} \leq 1$, $j = 1, 2, \ldots, n_d$, and the intermediate computational domain $-1 \leq x \leq 1$. The origin $r = 0$ is the locus of the black hole.

The mapping (29) allows the definition of the rational Chebyshev polynomials [34], which are the rescaled Chebyshev polynomials. In other words,

$$TL_k(r) = T_k\left(x = \frac{r - L_0}{r + L_0}\right), \tag{30}$$

where we obtain $x = x(r)$ after inverting the relation (29). The resulting basis function is now defined in the whole spatial domain. For the case of multiple subdomains, we define rational Chebyshev polynomials associated with each subdomain symbolically as [35]

$$TL_k^{(l)}(r) = T_k(\xi^{(l)}(r)). \tag{31}$$

We obtain the relation $\xi^{(l)} = \xi^{(l)}(r)$ after inverting the linear relation between x and $\xi^{(l)}$ and combining with Eq. (29).

When implementing the spectral code with the Galerkin-Collocation method, we consider the whole spatial domain, where the boundaries are the origin $r = 0$ and the spatial infinity. A distinctive aspect of our implementation is establishing basis functions that enforce the boundary conditions. For instance, for the case of spacetimes initially without black holes (see Refs. [36,39,40]), the BSSN equations in spherical coordinates have $1/r$ terms near the origin that require a proper process of regularization. It is possible, as we have shown [36], to define radial basis functions to behave as constant $+ \mathcal{O}(r^2)$ near the origin. However, the regularization procedure fails here due to a singularity at the origin [39].

The simplest solution is the cornerstone of treating black holes as punctures without excision. We exclude the origin from the spatial domain; consequently, we do not impose any particular conditions on the basis functions at the puncture even though the new conformal factor $\chi(t, r)$ is regular [cf. Eq. (16)]. Thus, the spectral approximations can vary in the neighborhood of the puncture to deal with the $1/r$, $1/r^2$ terms near it.

The only condition we must enforce is guaranteeing that the spacetime is asymptotically flat. Taking the rational Chebyshev polynomials [Eq. (30)] in one domain or the polynomials $TL_k^{(n_d)}(r)$ [Eq. (31)] in the outer subdomain (see the discussion in the sequence), we define the new basis function $\psi_k(r)$ as

$$\psi_k(r) \equiv \frac{1}{2}(TL_{k+1}(r) - TL_k(r)). \tag{32}$$

Since $TL_k(r) = (-1)^k + \mathcal{O}(r^{-1})$ asymptotically, it follows that $\psi_k(r) = \mathcal{O}(r^{-1})$.

At this point, by restricting to the single-domain case, we can write the spectral approximations for the field variables. The requirement of asymptotic flatness implies the following conditions for two groups of field functions:

$$a, b, \alpha, \chi \to 1 \text{ as } r \to \infty, \tag{33}$$

$$\beta, \bar{\Delta}^r, K, A_a \to 0 \text{ as } r \to \infty. \tag{34}$$

Thus, for the first group, we have

$$\chi(t, r) = 1 + \sum_{k=0}^{N} \hat{\chi}_k(t)\psi_k(r), \tag{35}$$

and similar expansions for the metric functions a, b and the lapse α. Here N is the truncation order that dictates the number of unknown coefficients or modes $\hat{\chi}_k$. For the second group, it follows

$$K(t, r) = \sum_{k=0}^{N} \hat{K}_k(t)\psi_k(r), \tag{36}$$

where $\hat{K}_k(t)$ are the correspondent modes associated with the trace of the extrinsic curvature. Again, we have similar expansions for the remaining functions of the second group.

The next step is determining the modes present in the spectral approximations for both groups of functions. After substituting all spectral approximations into the field equations, we obtain the corresponding residual BSSN equations. For the sake of illustration, let us consider the residual equation associated with the new conformal factor χ:

$$\mathrm{Res}_\chi(t, r) = \partial_t\chi - \beta^r\partial_r\chi + \frac{n}{6}\chi\bar{\nabla}_k\beta^k - \frac{n}{6}\chi\alpha K. \tag{37}$$

Notice that $\mathrm{Res}_\chi(t, r)$ does not vanish due to the inserted approximations. Then, following the prescription of the collocation method, we impose that the residual equation (37) vanishes at the $N + 1$ collocation points r_j. Then, $\mathrm{Res}_\chi(t, r_j) = 0$ constitutes the set of $N + 1$ equations

$$(\partial_t\chi)_j = (\beta^r\partial_r\chi)_j - \frac{n}{6}\chi_j(\bar{\nabla}_k\beta^k)_j + \frac{n}{6}\chi_j\alpha_j K_j, \tag{38}$$

where the subscript j indicates that we evaluate the quantities at the collocation point r_j. From the above set of equations, we can calculate the values $\chi_j(t)$ at the next time level, provided the rhs is known. The values of the conformal factor $\chi_j(t)$ and its modes $\bar{\chi}_k(t)$ are connected through

$$\chi_j(t) \equiv \chi(t, r_j) = 1 + \sum_k \hat{\chi}_k(t)\psi_k(r_j)$$

so that we can determine the modes $\hat{\chi}_k(t)$ at any instant. Here, the $N + 1$ collocation points are initially defined in the computational domain $-1 \leq x \leq 1$, usually as the Chebyshev-Gauss-Lobatto points

$$x_j = \cos\left(\frac{j\pi}{N + 2}\right), \quad j = 1, 2, \ldots, N + 1, \tag{39}$$

where the points $x = -1$ ($j = N + 2$) and $x = 1$ ($j = 0$) are excluded, meaning that the origin and the spatial infinity are excluded. The points in the physical domain become

$$r_j = L_0\frac{(1 - x_j)}{1 + x_j}, \quad j = 1, 2, \ldots, N + 1. \tag{40}$$

After performing the same procedure described above on the remaining BSSN field equations, we approximate them as ordinary differential equations for the values of the field functions at the collocation points, $\chi_j, \beta^r_j, K_j, \ldots$. We obtain the initial values and corresponding initial modes by specifying the initial configuration for each field. Consequently, the rhs of each approximate equation is known initially, implying that we can determine the values at the next time level. Repeating this process iteratively, we evolve the set of equations, or equivalently the spacetime. Symbolically, the resulting set of approximate BSSN equations are

$$(\partial_t F)_j = G_j, \tag{41}$$

where $j = 1, 2, \ldots, N + 1$, and F represents all field functions: $\chi, a, b, K, A_a, \bar{\Delta}^r, \alpha, \beta, B$. The rhs is formed by the field functions' values and their spatial derivatives' values at the collocation points.

Maximal slicing: We also have implemented a version of the spectral code with the maximal slicing gauge [45]. In this case, we have

$$K = \partial_t K = 0. \tag{42}$$

Consequently, the lapse does not satisfy a gauge evolution equation, but rather an elliptic-type equation given by

$$\partial_r^2 \alpha - \left(\frac{2}{r} - \frac{\partial_r a}{2a} + \frac{\partial_r b}{b} - \frac{2\partial_r \chi}{n\chi} \right) \partial_r \alpha - \frac{3}{2} \alpha a \chi^{-4/n} A_a^2 = 0. \tag{43}$$

From the spectral perspective, we have approximated this equation by a set of linear algebraic equations for the values of the lapse $\alpha_j(t)$, $j = 1, 2, \ldots, N+1$. We solve this equation in each interaction by the standard matrix inversion. The procedure described previously for all other functions is not altered.

Multidomain Galekin collocation method: In the case of the multidomain implementation, we first establish spectral approximations for the field functions of both groups in each subdomain. In the subdomains $\mathcal{D}_1, \mathcal{D}_2, \ldots, \mathcal{D}_{n_d-1}$, the basis functions are the corresponding rational Chebyshev polynomials $TL_k^{(l)}(r)$, whereas for the outer subdomain $\mathcal{D}_{n_d}: r^{(n_d-1)} \leq r < \infty$, the basis functions are

$$\psi_k^{(n_d)}(r) = \frac{1}{2}(TL_{k+1}^{(n)}(r) - TL_k^{(n)}(r)). \tag{44}$$

In general, the truncation orders or the number of modes for each field function, $N^{(l)}, l = 1, 2, \ldots, n_d$, are freely chosen, but unless stated otherwise, we have set the same truncation order for all functions.

The procedure to approximate the BSSN field equations is similar to what we have done in a single domain. We have to establish spectral approximations for the functions in each subdomain. For instance, considering the new conformal factor, we have

$$\chi^{(l)}(t, r) = 1 + \sum_{k=0}^{N^{(l)}} \hat{\chi}_k^{(l)}(t) \psi_k^{(l)}(r), \tag{45}$$

where $\hat{\chi}_k^{(l)}(t)$ are the modes and $l = 1, 2, \ldots, n$ indicates the subdomain, and $k = 0, 1, \ldots, N^{(l)}$.

Next, after obtaining the residual equations in each subdomain, we impose that these equations vanish at the collocation points of the corresponding subdomains. However, we must guarantee that each subdomain's functions' approximations represent the same functions defined in distinct subdomains. To this aim, the spectral approximations must satisfy the transmission conditions [46,47]

$$\chi^{(l)}(t, r^{(l)}) = \chi^{(l+1)}(t, r^{(l)}),$$
$$\left(\frac{\partial \chi}{\partial r}\right)_{r^{(l)}}^{(l)} = \left(\frac{\partial \chi}{\partial r}\right)_{r^{(l)}}^{(l+1)}, \tag{46}$$

TABLE I. Distribution of the collocation points in each subdomain according to corresponding truncation orders.

$\mathcal{D}_1$	$\mathcal{D}_2$	$\cdots$	$\mathcal{D}_{n_d-1}$	$\mathcal{D}_{n_d}$
$N^{(1)}$	$N^{(2)} - 1$	$\cdots$	$N^{(n_d-1)} - 1$	$N^{(n_d)}$

with $l = 1, 2, \ldots, n_d - 1$. Consequently, the number of transmission conditions restricts the total number of collocation points. For instance, if we have n_d subdomains, the total number of modes is

$$\sum_{l=1}^{n_d} N^{(l)} + n_d,$$

and with $2(n_d - 1)$ transmission conditions, the effective number of values is

$$\sum_{l=0}^{n_d} N^{(l)} - n_d + 2.$$

The above number of values coincides with the total number of collocation points distributed along the subdomains, and therefore, the total number of equations represented by Eq. (41). In Table I [35], we show the distribution of the collocation points in each subdomain.

We approximate the BSSN equations as a set of differential equations for the values of the field functions at the collocation points as the final step of the implementation. We can summarize these equations as

$$(\partial_t F)_j^{(l)} = G_j^{(l)}, \tag{47}$$

where $F^{(l)}$ represents all field functions in each subdomain, $j = 1, 2, \ldots, \bar{N}^{(l)}$, with $\bar{N}^{(l)}$ being the number of collocation points in the lth subdomain, and $l = 1, 2, \ldots, n_d$.

The implementation of the maximal slicing version is straightforward. It follows the same procedure described above for all functions, and the lapse satisfies Eq. (43) in each subdomain, which we solve to obtain the values $\alpha_j^{(l)}, = 1, 2, \ldots, N^{(l)}$.

IV. NUMERICAL RESULTS

We present the numerical tests used to validate the domain decomposition GC code for describing punctures without excision, where we have proposed three groups of numerical experiments. The first group verifies some relevant solutions of the Schwarzschild black hole in distinct foliations or geometries. We explore the transition from the wormhole to trumpet foliations [44,48,49] in connection with the moving puncture approach in the second group. In the third group, we consider the description of the power-law behavior near the puncture after the establishment of the trumpet stationary configuration.

We have integrated the resulting dynamical systems [Eqs. (41) and (47)] with the Cash-Karp adaptive step-size integrator [50] in all numerical experiments. We choose $n = 2$ for the conformal factor [Eq. (16)], the maximum step size is 10^{-4}, and the tolerance is in the interval 10^{-13} to 10^{-13}.

A. Testing the code with exact solutions

We start with the standard exact Schwarzschild black hole solution expressed in a wormhole geometry or foliation:

$$ds^2 = -\left(\frac{1-\frac{M}{2r}}{1+\frac{M}{2r}}\right)^2 dt^2 + \left(1+\frac{M}{2r}\right)^4 (dr^2 + r^2 d\Omega^2), \quad (48)$$

where M is the black hole mass. The above metric is an exact time-independent solution. Therefore, if we use it as the initial configuration to feed the BSSN equation, we would be able to verify the Schwarzschild solution's static character numerically. However, as pointed out in Ref. [49], the negative values of the lapse for $r < M/2$ leads, in general, to numerical instabilities.

We evolve the solution (48) as the initial data with the nonadvective $1 + \log$ slicing condition for the lapse and the gamma-driver condition with $\eta = 0$ for the shift in Eq. (25), respectively. As a result, the numerical solution crashes after a few time units, say $t \sim \mathcal{O}(10M)$. We repeat the same experiment using Alcubierre's gauge shock-avoiding slicing [27]

$$f(\alpha) = 1 + \frac{\kappa_0}{\alpha^2}, \quad (49)$$

where for the sake of convenience, we have set $\kappa_0 = 2/3$. We observe the growth of instabilities again, but at a much slower rate. Figure 2 shows the log-linear plots of the Hamiltonian constraint violation expressed by its L_2 norm, henceforth denoted by $L_2(HC)$, for an integration until $t = 40M$ with truncation orders $N = 50$, 70, 90, and map parameter $L_0 = 5M$. Despite the increase in the error, the advantage of the slicing condition (49) is clear in providing a better agreement with the exact solution. As shown in Fig. 2, $L_2(HC) \sim \mathcal{O}(10^{-9})$ for $N = 90$. Eventually, for longer integration times, the numerical solution crashes. An explanation for a better performance of the Alcubierre's $f(\alpha)$ is that the term $\alpha^2 f(\alpha)$ is always positive, even though the lapse assumes negative values for $r < M/2$.

We have examined the following analytical solution due to Dennison and Baumgarte [51] representing the Schwarzschild black hole in a trumpet geometry:

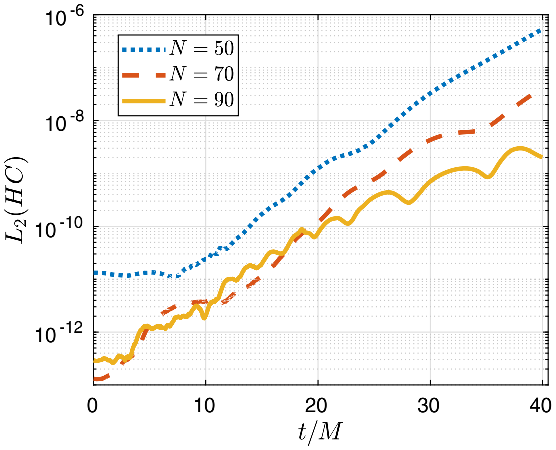

FIG. 2. Time evolution of the Hamiltonian constraint evolution with the truncation orders $N = 50$, 70 and 90. The initial data are for the Schwarzschild solution [Eq. (48)], where we evolve the lapse nonadvecting condition with Alcubierre's shock-avoiding slicing [Eq. (49)], $\eta = 0$ in the gamma-driver condition, and map parameter $L_0 = 5M$.

$$ds^2 = -\left(\frac{r}{r+M}\right)^2 dt^2 + \frac{2rM}{(r+M)^2} dr dt + \left(1+\frac{M}{r}\right)^2 (dr^2 + r^2 d\Omega^2). \quad (50)$$

In addition, the trace of the extrinsic curvature and the component A_a are given by [51]

$$K = \frac{M}{(r+M)^2}, \qquad A_a = -\frac{4M}{3(r+M)^2}. \quad (51)$$

With the metric (50) and the above expressions, we establish the initial data to integrate the BSSN equations. In this case, the Bona-Massó function $f(\alpha)$ is [51]

$$f(\alpha) = \frac{1-\alpha}{\alpha}, \quad (52)$$

together with the advective lapse [Eq. (25)]. We present in Fig. 3 the time evolution of the L_2 norm of the Hamiltonian constraint instead of comparing the exact and the analytical metric functions. We have set the truncation order $N = 70$, the map parameter $L_0 = 5$, and evolved the system until $t = 40M$. The error remains at about $\mathcal{O}(10^{-13})$ after $t \sim 15M$.

The third analytical solution we have considered is the maximal slicing Schwarzschild black hole [53]. For convenience, we use the explicit analytical expressions in isotropic coordinates obtained by Baumgarte and Naculich [52] to generate the initial data. Then, with the spatial line element

$$\gamma_{ij} dx^i dx^j = \Psi^4 (dr^2 + r^2 d\Omega^2), \quad (53)$$

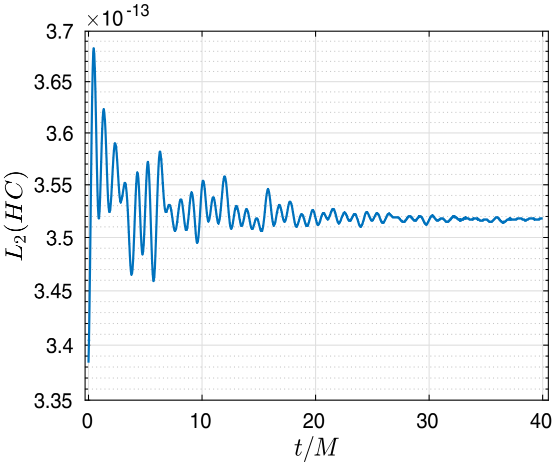

FIG. 3. Time evolution of the Hamiltonian constraint violation with the exact solution [Eqs. (50) and (51)] [52] taken as the initial data. We evolve the lapse with the advective condition with $f(\alpha)$ given by Eq. (52), $\eta = 0$ in the gamma-driver condition, and map parameter $L_0 = 5M$.

it follows that the conformal factor is

$$\Psi = \left(\frac{R}{r}\right)^{1/2} = \left[\frac{4R}{2R + M + (4R^2 + 4MR + 3M^3)^{1/2}}\right]^{1/2} \times \left[\frac{8R + 6M + 3(8R^2 + 8MR + 6M^2)^{1/2}}{(4 + 3\sqrt{2})(2R - 3M)}\right]^{1/2\sqrt{2}}. \quad (54)$$

Here, R is the areal coordinate with a limiting value of $3M/2$ when the isotropic radial coordinate r approaches zero. The lapse and the shift are, respectively, given by

$$\alpha = \left(1 - \frac{2M}{R} + \frac{27M^4}{16R^4}\right)^{1/2}, \quad (55)$$

$$\beta^r = \frac{3\sqrt{3}M^2}{4}\frac{r}{R^3}. \quad (56)$$

The collocation points are expressed in terms of the isotropic coordinate r, but by inverting the relation $r = r(R)$ [cf. Eq. (54)], we obtain the corresponding points in the areal coordinate R. Consequently, we generate the initial values of the conformal factor χ_j, the lapse α_j, and the shift β^r_j, with $j = 1, 2, \ldots, N+1$. For the remaining fields, we have initially $a = b = 1, K = \bar{\Delta}^r = 0$.

We present in Fig. 4(a) the time behavior of $L_2(HC)$ for the truncation orders $N = 50$, 70, 90, 110, 150, and 190 with map parameter $L_0 = 5M$, the nonadvecting $1 + \log$ slicing, and $\eta = 0$ for the gamma-driver condition. We notice that $L_2(HC)$ decays as the resolution increases, but for a more precise determination of its decay rate, we have calculated the rms value of $L_2(HC)$ for each truncation order N. In Fig. 4(b), we present the log-log plot for the map parameters $L_0/M = 2, 5$. In both cases, we observe an algebraic rather than exponential decay.

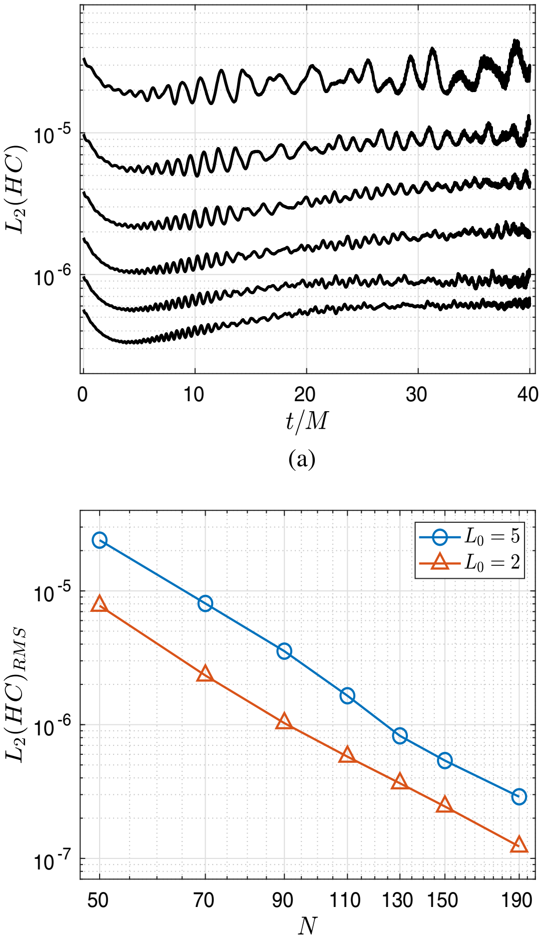

(a)

(b)

FIG. 4. (a) Log-linear plots of $L_2(HC)$ vs time for the truncation orders $N = 50$, 70, 90, 110, 130, 150, and 190 from top to bottom. The initial data are for the analytical Baumgarte-Naculich solution [52], and we evolve the lapse with the non-advecting $1 + \log$ slicing, with $\eta = 0$ for the gamma-driver condition, and the map parameter is $L_0 = 5M$. (b) Log-log plots of $L_2(HC)_{\mathrm{RMS}}$, showing its algebraic decay with the increase of the truncation order, where the map parameters are $L_0/M = 2, 5$.

The $1/r^2$, $1/r$ terms near the puncture and present in Hamiltonian constraint, and some of the evolution equations, spoil the usual exponential convergence. Nevertheless, the rms value decreases by 2 orders of magnitude for $L_0 = 2M$ when the number of collocation points increases from 50 to 190. In our judgment, the cost of letting the spectral approximations remain free near the puncture is worth it.

We repeat the same numerical test with Alcubierre's shock-avoiding gauge $f(\alpha)$ [Eq. (49)] ($\kappa_0 = 2/3$) and the maximal slicing spectral code. In all simulations, we have set $L_0 = 2M$ and truncation orders $N = 70, 90, \ldots, 190$. To compare the outcomes of distinct gauge conditions, we have plotted in Fig. 5 the decay of the rms values of the

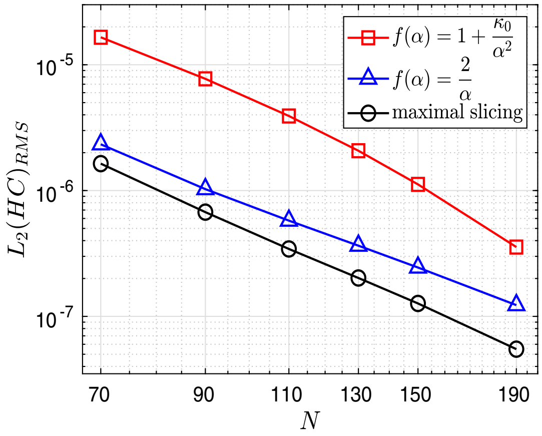

FIG. 5. Algebraic decay of $L_2(HC)_{\mathrm{RMS}}$ for the Alcubierre slicing [Eq. (49)] with $\kappa_0 = 2/3$ (squares), $1 + \log$ slicing (triangles), and the maximal slicing version of the code (circles). Here, $L_0 = 2M$.

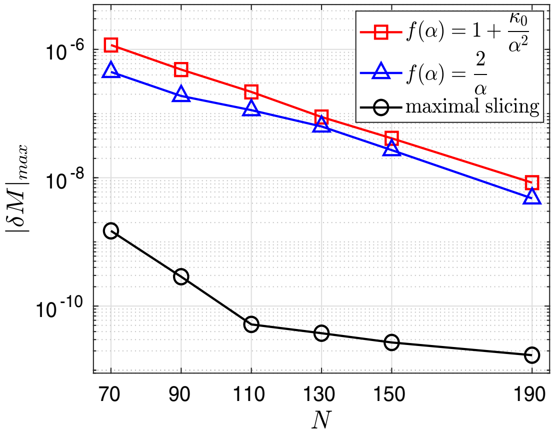

FIG. 6. Exponential convergence of the ADM mass's maximum deviation for the Alcubierre shock-avoidance slicing [Eq. (49)] with $\kappa_0 = 2/3$ (squares), the $1 + \log$ slicing (triangles), and the maximal slicing version of the code (circles). Here, $L_0 = 2M$.

error $L_2(HC)$ for simulations until $t = 40M$, including the $1 + \log$ slicing. Although the individual rms values obtained using Eq. (49) are greater than the corresponding values for the maximal and $1 + \log$ slicing, its decay seems slightly faster than the algebraic decay. The maximal slicing presents the best outcome.

Another valid test is the convergence of the ADM mass. The spectral approximation of the field functions offers a global description of the related functions. We use this feature to calculate the ADM mass straightforwardly. Due to the asymptotic flatness of spacetime, we can write

$$\mathrm{e}^{\phi} = (\chi)^{-1/n} = 1 + \frac{M_{\mathrm{ADM}}}{2r} + \mathcal{O}(r^{-2}), \tag{57}$$

where M_{ADM} is the ADM mass of the system. Using the spectral approximation in Eq. (35) for the new conformal factor and taking into account the asymptotic form of the basis functions, we can express the ADM mass in terms of the unknown modes $\hat{\chi}_k$ as

$$M_{\mathrm{ADM}} = \frac{2\chi_{-1}}{n} = \frac{8}{n}\sum_{k=0}^{N}(2k-1)\hat{\chi}_k(t), \tag{58}$$

where χ_{-1} is the coefficient of the $1/r$ term for the asymptotic form of the approximate conformal factor [Eq. (35)].

Figure 6 shows the convergence of the maximum deviation of the ADM mass $\delta M = M_{\mathrm{ADM}}(0) - M_{\mathrm{ADM}}(t)$, since the numerical ADM mass varies with time. In all cases, the exponential decay of $|\delta M|_{\max}$ is restored, with similar results for $f(\alpha)$ given by Eq. (49) and the $1 + \log$ slice, where the maximal deviation reaches less than 1 part in 10^8. The maximal slicing code exhibits a much better convergence if compared with the previous choices of $f(\alpha)$. To explain the exponential convergence, we recall that the ADM mass is a quantity evaluated far from the puncture. Therefore, we infer that the numerical errors produced near the puncture have a reduced influence on the ADM mass value. It represents "a spectral" confirmation of one of the main features of the moving puncture approach, where the errors only affect the neighborhood of the puncture [41].

B. Transition from the wormhole to trumpet geometries

We explore the transition of the Schwarzschild black hole from the wormhole to trumpet geometries [44,48,49] that arises in connection with the moving puncture approach. We have considered the multidomain version of the spectral code for the numerical experiments and the maximal slicing version for this aim. We characterize the initial data by the spatial line element given by Eq. (53) with the conformal factor

$$\Psi_0 = 1 + \frac{M}{2r}, \tag{59}$$

together with $K_{ij} = 0$. In addition, we assume the initial precollapsed lapse

$$\alpha = \Psi_0^{-2}. \tag{60}$$

We remark that the initial condition for the lapse is no longer necessary for the maximal slicing code.

We evolve the lapse with the nonadvective form of Eq. (25) together with Alcubierre's family $f(\alpha)$, given by Eq. (49) and

$$f(\alpha) = \frac{k_0}{\alpha}, \tag{61}$$

$$f(\alpha) = \frac{\kappa_0^2}{2\alpha + (\kappa_0 - 2)\alpha^2}, \tag{62}$$

where the former is the generalization of the $1 + \log$ slicing ($k_0 = 2$), and the latter was proposed by Alcubierre [28] after imposing zeroth-order shock avoidance. In this case, we recover the $1 + \log$ slicing condition for $\kappa_0 = 2$.

In all simulations, except with the maximal slicing code, we have employed a spectral filter [54] to prevent the growth of higher frequencies that spoil the accuracy of the numerical solution. At each time step, we have applied an exponential filter only to the modes of the extrinsic curvature for simplicity and functionality. Trying, for instance, to filter the modes of the metric functions $a(t, r)$ or $b(t, r)$ breaks the stability of the numerical integration. We intend to address this issue in more detail elsewhere.

The rms value of the L_2 norms of the Hamiltonian constraint violation calculated in each subdomain and denoted by $L_2(HC_i)_{\rm RMS}$, $i = 1, 2\ldots, n_d$ signalize the convergence and accuracy of the code. Another quantity with this aim is the deviation of the ADM mass from its initial value. We determine the ADM mass in each instant with

$$M_{\rm ADM} = \frac{8}{n}\sum_{k=0}^{N^{(n_d)}}(2k-1)\hat{\chi}_k^{(n_d)}(t), \tag{63}$$

where $\hat{\chi}_k^{(n_d)}(t)$ are the unknown modes associated with the conformal factor $\chi(t, r)$ in the outer subdmain $\mathcal{D}_{n_d}: r^{(n_d)} \leq r < \infty$.

The first numerical experiment illustrates the evolution of the Hamiltonian constraint violation in the first subdomain represented by its L_2 norm, $L_2(HC_1)$, for the two-subdomain maximal slicing code with $N^{(1)} = N^{(2)} = 110$, i.e., with 110 collocation points in each subdomain. We have set $r^{(1)} = L_0 = 5M$ [$x^{(1)} = 0$ in the intermediary computational domain] and $\eta = 2$ for the gamma-driver condition. The first subdomain contains the black hole interior $r_H < 2M$. In Fig. 7, we show the Hamiltonian constraint violation until $t = 40M$, and in the inset, the whole evolution until $= 100M$ to illustrate the achievement of the stationary phase.

In the sequence, we exhibit the convergence of the L_2 norms of the Hamiltonian constraints in both subdomains. We have performed the numerical experiments with the families $f(\alpha)$ given previously and the maximal slice code. We set $k_0 = 2$ or $1 + \log$ gauge in Eq. (61), with $\kappa_0 = 2/3$ and $\kappa_0 = 1.7635$ for the Alcubierre families in Eqs. (49) and (62), respectively [29]. The map parameter is $L_0 = 5M$, and $\eta = 2$ for the gamma-driver condition in all simulations.

Figure 8 shows the decay of the rms values of $L_2(HC_i)$, with $i = 1$, 2 for the truncation orders $N^{(1)} = N^{(2)} = 70$, 110, 150, 190, and 230. In the first subdomain $\mathcal{D}_1: 0 < r \leq r^{(1)} = 5M$, the decay of $L_2(HC_1)_{\rm RMS}$ is algebraic and almost the same in all slicing conditions [the results provided by the family in Eq. (49) are similar to the other cases]. The errors near the puncture considerably violate the Hamiltonian constraint and spoil the exponential convergence.

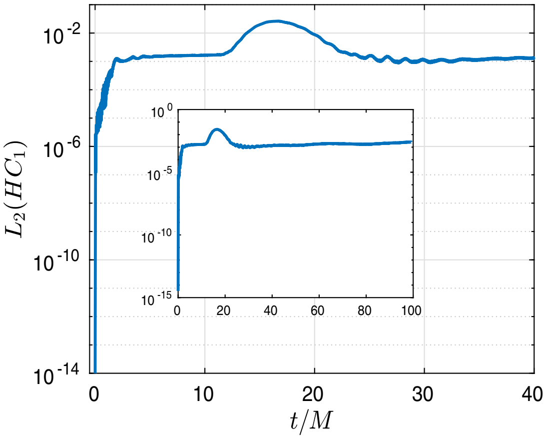

FIG. 7. Time evolution of the Hamiltonian constraint violation in the first subdomain for the integration until $t = 40M$, and the inset shows the time evolution until $t = 100M$ to illustrate the achievement of the stationary phase after $t \simeq 30M$. We have used the maximal slicing code with $N^{(1)} = N^{(2)} = 110$, $r^{(1)} = L0 = 5M$, and $\eta = 2$ for the gamma-driver condition.

When we turn to the second subdomain, we obtain an evident exponential decay of $L_2(HC_2)_{\rm RMS}$ for the maximal slicing code (black circles), with saturation taking place at $L_2(HC_2)_{\rm RMS} \sim \mathcal{O}(10^{-7})$. The simulations with the families in Eqs. (61) and (62) (blue triangles and red squares, respectively) show better accuracy with a satisfactory decay rate, albeit not exponential; the minimum of $L_2(HC_2)_{\rm RMS}$ is the same as that obtained with the maximal slicing code. The simulations with the family in Eq. (49) with $\kappa_0 = 2/3$ yield a slower convergence rate, but with acceptable violations of the Hamiltonian constraint. We recall that the second subdomain $\mathcal{D}_2: 5M \leq r < \infty$, meaning that all the collocation points are outside the horizon and away from the puncture, this therefore being the main reason for the improvement of the convergence and accuracy of the results.

We illustrate the effect of filtering in the decay of $L_2(HC_2)_{\rm RMS}$ with $1 + \log$ slicing. The dashed curve on the top of Fig. 8(b) with blue triangles refers to the absence of filtering in contrast to the results obtained with a filter (triangles with solid line). The improvement in the accuracy is about 3 orders of magnitude.

We include the convergence of the ADM mass expressed by its maximum deviation in Fig. 9. The log-linear plots of $|\delta M|_{\rm max}$ indicate a rapid convergence in all cases, with the outcome due to the maximal slicing code displaying a much better convergence.

As a qualitative test, we present two illustrations showing the approaches to stationary trumpet geometries through snapshots of the shift in distinct instants, where $\beta^r = 0$ initially. In both illustrations, we have used a two-subdomain code with the nonadvective $1 + \log$ slicing

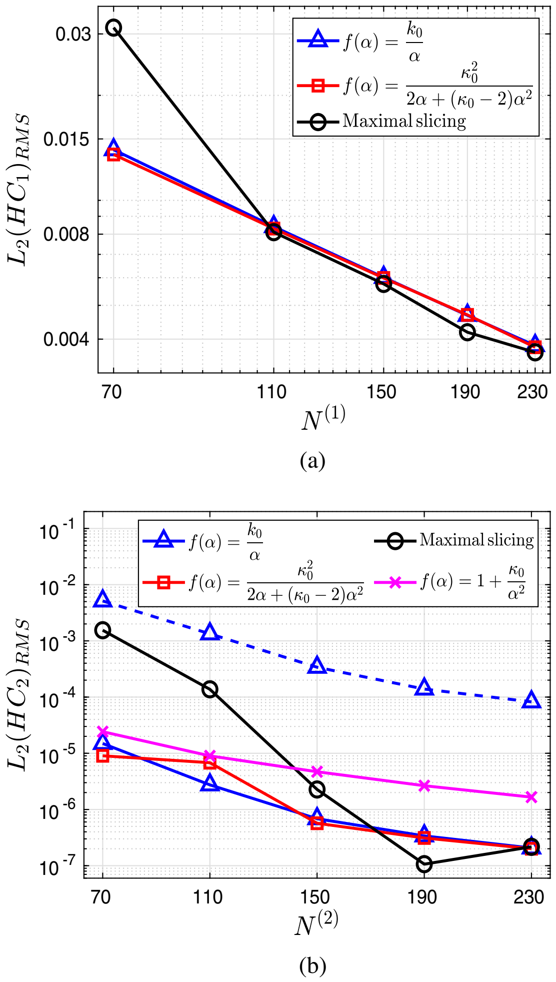

FIG. 8. (a) Algebraic decay of $L_2(HC_1)_{\rm RMS}$ using the $1 + \log$ slicing ($k_0 = 2$), the Alcubierre zeroth-order shock-avoidance slicing with $\kappa_0 = 1.7635$ in Eq. (62), and the maximal slicing. (b) The log-linear plot of $L_2(HC_2)_{\rm RMS}$ includes the Alcubierre shock-avoidance slicing [Eq. (49)] with $\kappa_0 = 2/3$. The dashed line with triangles at the top refers to the rms values obtained without filtering. We have fixed the map parameter $L_0 = 5M$ and $\eta = 2$ for the gamma-driver condition. The interface separating both subdomains is located at $r_{(1)} = L_0 = 5M$.

condition for the lapse. We set $n = 2$ for the new conformal factor, with the map parameter $L_0 = 5M$, and the interface located at $r^{(1)} = L_0$.

In the first illustration, we have chosen $\eta = 2$ and truncation orders $N^{(1)} = N^{(2)} = 150$. Figure 10 shows the snapshots of the shift in four different instants, namely $t/M = 1.4, 3.2, 15, 38$ with dotted, dashed, dot-dashed and solid lines, respectively, where the simulation ends at $t/M = 40$. We notice that at $t/M = 15$, the shift is close to the stationary configuration represented by the solid line ($t/M = 38$). After $t/M \simeq 25$, the curves become superposed to the solid line shown in Fig. 10.

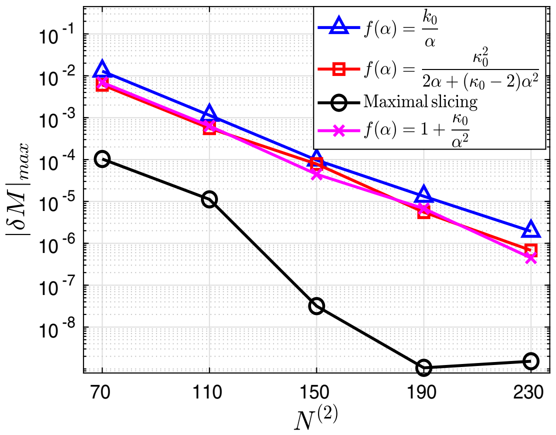

FIG. 9. Exponential convergence of the ADM mass's maximum deviation for the Alcubierre slicings in Eqs. (49) and (62) with $\kappa_0 = 2/3$ and 1.7635, respectively, the $1 + \log$ slicing ($k_0 = 2$), and the maximal slicing version of the code. Here, $L_0 = 5M$.

For the second sequence of profiles of the shift towards the equilibrium configuration, we have used more resolution, $N^{(1)} = N^{(2)} = 190$, and fixed $\eta = 0$. As a result, we plot seven panels in distinct instants in Fig. 11, namely $t/M = 1.4$, 3.5, 5.6, 12.4, 14.9, 21.6, and 37.7. In each panel, the black dashed line represents the exact solution for the shift vector [52] for which the numerical solution settles. We notice that the distinct equilibrium configurations of the shift shown by Figs. 10 and 11 reflect the action of the parameter η in changing the coordinates of the final slice, but not the slice [44,55,56].

We end the present subsection by repeating the same convergence tests using a three-subdomain code with the $1 + \log$ gauge [$k_0 = 2$ in Eq. (61)] and the two Alcubierre families in Eqs. (49) and (62), in which $\kappa_0 = 2/3$ and 1.7365, respectively. The interfaces are located at $r^{(1)} = L_0/2$ and $r^{(2)} = 2L_0$ ($x^{(1)} = -1/3$ and $x^{(2)} = 1/3$ in the

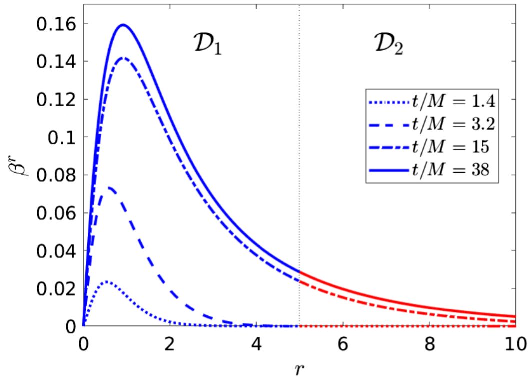

FIG. 10. Snapshots of the lapse β^r in different instants toward the equilibrium configuration at $t = 38M$ evolved with the initial wormhole data and the precollapsed lapse [Eq. (60)]. We adopt the nonadvective $1 + \log$ slicing condition for the lapse and the gamma-driver condition for the shift with $\eta = 2$ in the last equation. The vertical line indicates the interface between the subdomains.

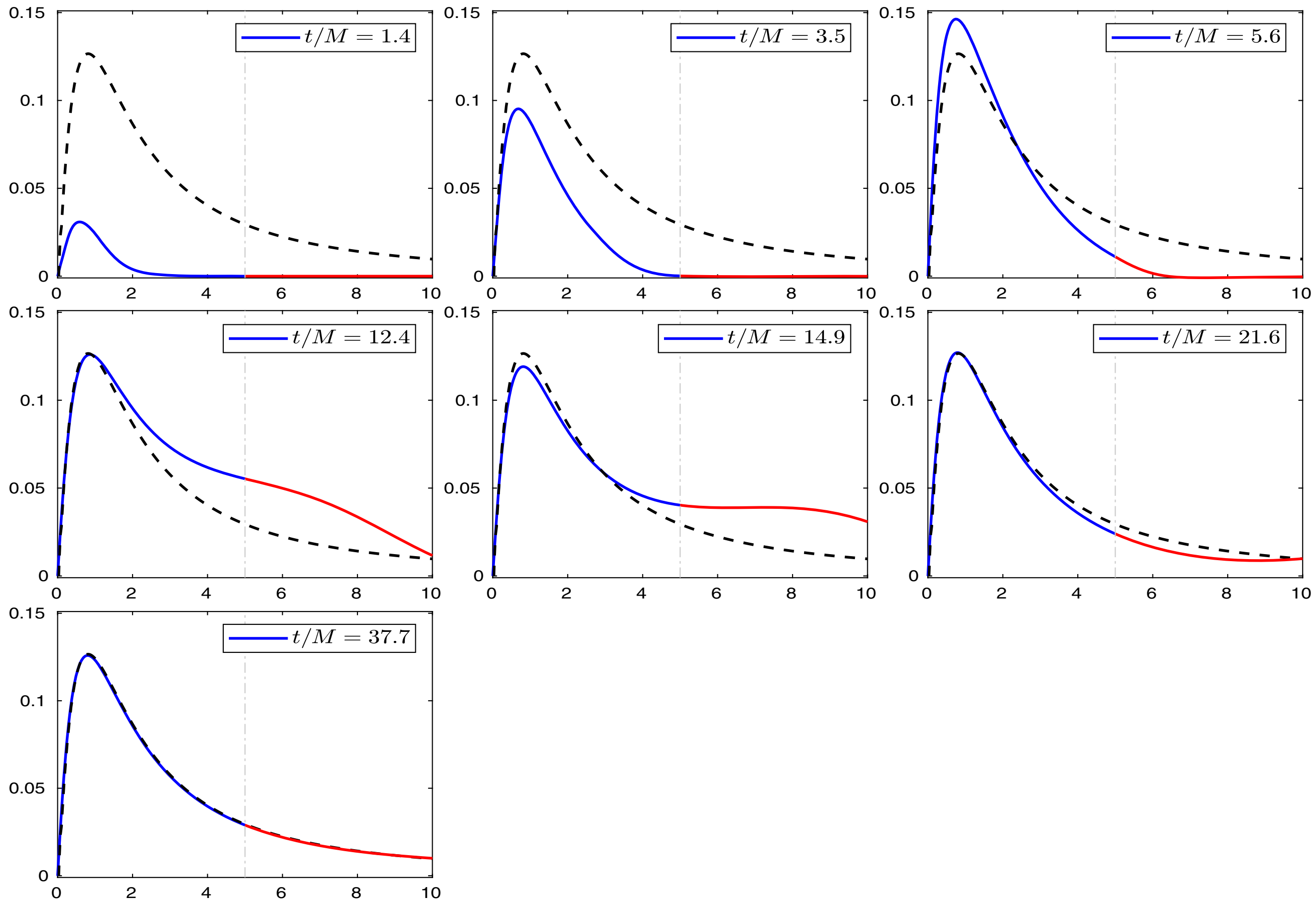

FIG. 11. Snapshots of the lapse β^r in different instants toward the equilibrium configuration represented [52] by the dashed line in each panel. The vertical line indicates the interface between the subdomains. The initial data are the same as in Fig. 10, but we set $\eta = 2$ in the gamma-driver condition.

intermediary computational domain). The truncation orders are equal in each subdomain; the map parameter is $L_0 = 10M$, and $\eta = 2$ is the gamma-driver condition.

In Fig. 12, we show the decay of the rms values of the L_2 norms of the Hamiltonian constraints in the first (top panel), second (center panel), and third (bottom panel) subdomains. As expected, the log-log plot in the first subdomain displays an algebraic convergence, since it encompasses the neighborhood of the puncture. In this instance, all families $f(\alpha)$ produce similar results.

The log-linear plots of $L_2(HC)_{\mathrm{RMS}}$ in the second and third subdomains reveal better convergence and more accurate results, with the slicing condition in Eq. (62) presenting superior performance if compared with the other slicing conditions. As expected, we regain a more closely related exponential convergence far from the puncture's neighborhood. Interestingly, the shock-avoiding slicing condition [Eq. (49)] with $\kappa_0 = 2/3$ produces inferior convergence and accuracy.

Finally, Fig. 13 depicts the convergence of the ADM mass with the decay of the maximum deviation $\delta M_{\max}$. All slicing conditions are similar, with the $1 + \log$ slicing slightly inferior to the others. We point out that for $N^{(3)} = 230$, the deviation of the ADM mass is about 1 part in 10^{10}.

C. Power-law behavior of the lapse near the puncture

In the last set of numerical experiments, we explore the power-law behavior of the lapse near the puncture. The initial data are the same for the transition of the Schwarzschild black hole from the wormhole to trumpet slices described in the previous subsection, and we evolve the lapse with the Bona-Massó condition [Eq. (25)]. In achieving the stationary configuration, the lapse exhibits a power-law behavior near the puncture [57], namely

$$\alpha \propto r^{1/\gamma}, \tag{64}$$

where the exponent $1/\gamma$ is determined analytically and depends on the choice for the function $f(\alpha)$ [29]. The objective is to show agreement between the lapse's analytical and numerical power-law behavior.

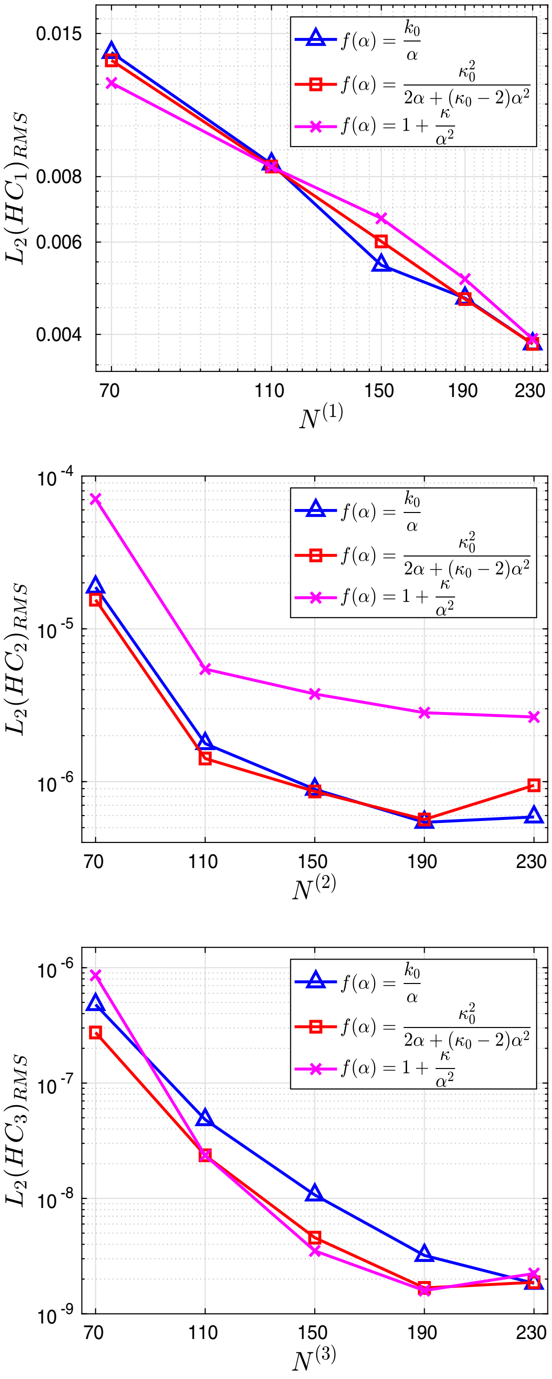

FIG. 12. The top, center, and bottom panels show the convergence of $L_2(HC)_{\rm RMS}$ in the first, second, and third subdomains, respectively. We have considered the maximal slicing, the Alcubierre slicing families in Eqs. (49) and (63) with $\kappa_0 = 2/3$ and 1.7635, respectively. The interfaces separating the subdomains are located at $r^{(1)}/M = 5$ and $r^{(2)}/M = 20$. In all cases, $\eta = 0$ for the gamma-driver condition.

We have considered the families of $f(\alpha)$ given by Eqs. (61) and (62), considering several values for the constants k_0 and κ_0. A three-subdomain code used previously with $N^{(1)} = N^{(2)} = N^{(3)} = 150$ collocation points is used to conduct the numerical experiments. We have also set $\eta = 2$ and the map parameter $L_0 = 10M$, yielding $r^{(1)} = 5M, r^{(2)} = 20M$ as the interface locations. The transition from wormhole to trumpet geometries generally settles approximately in $t = 30M$, but we have integrated until $t = 50M$ for the numerical experiments.

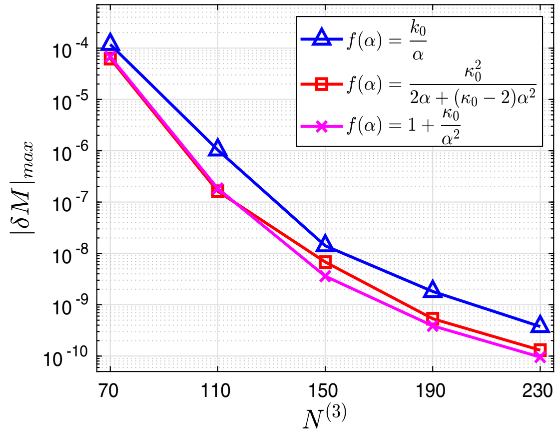

FIG. 13. Decay of the ADM mass's maximum deviation for the Alcubierre slicings in Eqs. (49) and (62) with $\kappa_0 = 2/3$ and 1.7635, respectively, the $1 + \log$ slicing ($k_0 = 2$), and the maximal slicing version of the code. Here, $L_0 = 10M$.

In Fig. 14, we present the profiles of the lapse, taking into account the generalized $1 + \log$ slicing $f(\alpha) = k_0/\alpha$ with the standard $1 + \log$ condition $k_0 = 2$, as well as $k_0 = 1.46263$ and $k_0 = 3.245$, which produce the power-law exponents $1/\gamma \simeq 1.091$, 1.0, and 1.201, respectively. We indicate in all graphs the subdomain's interfaces with dotted vertical lines and the innermost collocation point located at $r_{\rm inner} \simeq 3.655 \times 10^{-4}M$ with the dashed vertical line. We have also plotted all profiles on the same scale for the sake of comparison among all cases. By observing how the numerical profiles extend to the region $r \ll r_{\rm inner}$, the best case is $k_0 = 1.46263$ when the power-law exponent is approximately equal to unity. For $k_0 = 2$ ($1/\gamma \simeq 1.091$), we reproduce the power-law behavior accurately, but the lapse becomes negative at some point due to numerical errors. A similar and more accentuated feature is observed when $k_0 = 3.245$, for which $1/\gamma \simeq 1.201$.

We end this section by presenting the profiles of the lapse considering the second family [Eq. (61)] in Fig. 15 for two values of the free parameter: $\kappa_0 = 4/3$ and $\kappa_0 = 1.7365$. The corresponding power-law exponents are $1/\gamma \simeq 0.801$ and $1/\gamma \simeq 1.0$, respectively. As in the generalized $1 + \log$ family, the numerical scaling produces a better result for the integer exponent. However, we observe that the numerical scaling of Fig. 15's bottom panel extends to smaller radii than in the case of generalized $1 + \log$ $f(\alpha)$.

V. FINAL CONSIDERATIONS

In this paper, we have extended the Galerkin-Collocation multidomain decomposition technique to integrate the

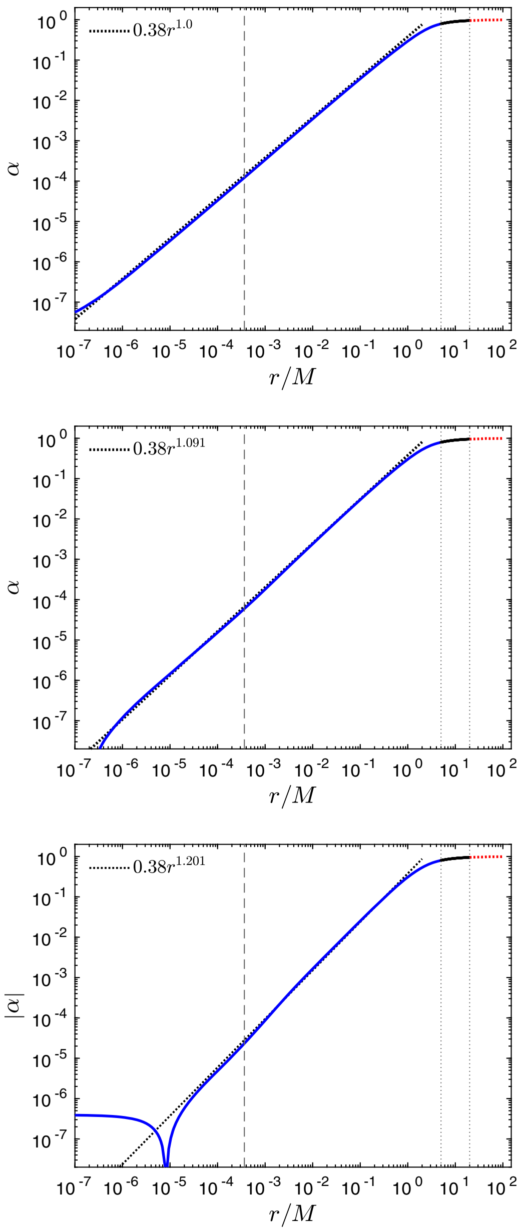

FIG. 14. Profiles of the lapse for the function $f(\alpha)$ given by Eq. (61), with $k_0 = 1.46263$, $k_0 = 2$ (1 + log slicing), and $k_0 = 3.245$ from the top to the bottom panels, respectively. The solid lines represent the numerical profiles of the lapse in the first subdomain, the vertical lines indicate the location of the innermost collocation point and the subdomain's interfaces, and the inclined straight dotted lines represent the scaling laws $r \propto r^{1/\gamma}$.

BSSN equations in spherical coordinates adapted to describe black holes represented by punctures without excision; we have also implemented a maximal slicing version of the code.

We have followed the standard strategy of previous implementations with the Galerkin-Collocation method. One of the main aspects of this method is constructing basis functions satisfying the boundary conditions individually.

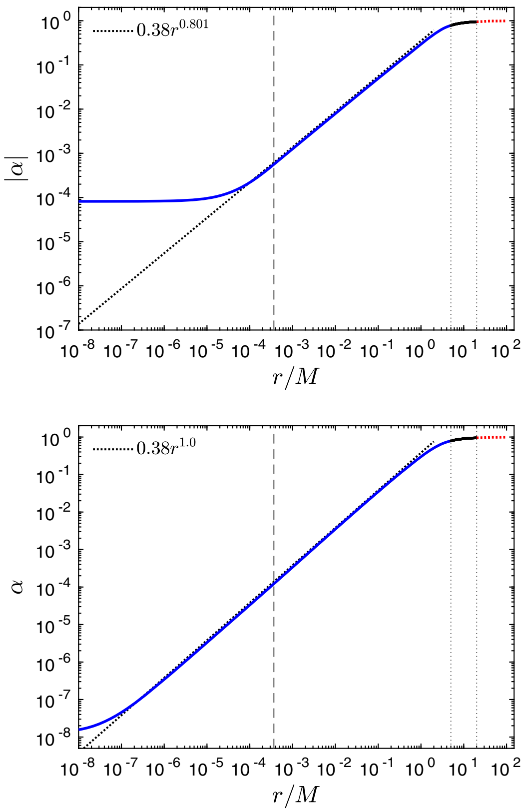

FIG. 15. Profiles of the lapse for the function $f(\alpha)$ given by Eq. (62) with $\kappa_0 = 4/3$ and $\kappa_0 = 1.7365$ in the top and the bottom panels, respectively. The solid lines represent the numerical profiles of the lapse in the first subdomain, the vertical lines indicate the location of the innermost collocation point and the subdomain's interfaces, and the inclined straight dotted lines represent the scaling laws $r \propto r^{1/\gamma}$.

Hence, we have combined the rational Chebyshev polynomials [34] to define basis functions to guarantee the asymptotic flatness. However, the locus of a black hole is a singularity, implying that it is ruled out from the spatial domain, meaning that we can no longer impose any special conditions regarding the basis functions at this point.

The simplest solution was not to impose regularity conditions near the puncture and let the spectral approximations deal with the $1/r$ and $1/r^2$ terms in the field equations close to the puncture. The numerical integration using finite differences adopts a similar strategy to deal with punctures [41]. On the other hand, we recall that the implementation of regularity conditions is mandatory for spacetimes initially without black holes [36,39,40].

We validate the code with three distinct numerical tests. The first is to examine the exact Schwarzschild solution in distinct foliations as initial data; namely, the wormhole solution in isotropic coordinates [cf. Eq. (48)], the analytical trumpet slices [51], and the Baumgarte-Naculich [52] analytical maximal slicing solution. The second test is to explore the transition from the wormhole to trumpet geometries starting with the "precollapsed" lapse [cf. Eq. (60)], and the third consists of verifying the power-law behavior of the lapse near the origin once we achieve the stationary trumpet configuration.

In all tests, we evolved the shift with the gamma-driver condition and the lapse with the Bona-Massó slicing condition. We have considered several slicing conditions, such as the standard $1 + \log$ slicing, and the two families of Alcubierre's shock-avoidance slicing [27,28], besides the maximal slicing in the numerical experiments. The determination of the time evolution of the Hamiltonian constraint violation through its L_2 norm and the verification of the ADM mass conservation constitutes the diagnostics for accuracy and convergence of the spectral code.

For the first set of numerical experiments, we have used a single-domain code, while for the remaining tests, we have used codes with two or three subdomains. Although the convergence dictated by the Hamiltonian constraint violation was algebraic, the correspondent L_2 norms' accuracy was entirely satisfactory. We have pointed out the influence of the numerical errors close to the puncture as the main factor for losing the standard exponential convergence. However, the convergence of the ADM mass measured by the decay of its maximum deviation δM_{max} with increased numerical resolution yields a much better outcome. Since the ADM mass is a quantity evaluated far from the puncture, it is not surprising that it is unaffected by the errors close to it. We have noticed the same feature when dealing with the Hamiltonian constraint violations in subdomains not containing the puncture.

Another aspect we have explored with the present code was the influence of distinct Bona-Massó functions [30]. The numerical experiments indicate that Alcubierre's zeroth-order slicing family [28] [cf. Eq. (62)] presents better results, but with the caveat that we must fix the constants present in the Bona-Massó functions.

Interestingly, the maximal slicing spectral code in a single domain and in two subdomains produced accurate and convergent results superior to those with the Bona-Massó slicing conditions.

We remark that the three-subdomain code accurately described the predicted power-law behavior of the lapse near the puncture after the evolution settles down into the stationary trumpet configuration. For those cases with integer exponents, the numerical solution reproduced the expected power-law behavior for r much smaller than the innermost collocation point.

Finally, the subsequent and natural development of the present research is to extend the spectral code to situations beyond the spherically symmetric spacetimes with or without black holes.

ACKNOWLEDGMENTS

H. P. O. acknowledges the hospitality of the Department of Physics and Astronomy of Bowdoin College. We thank T. Baumgarte for the discussions that resulted in the present work and for his comments and suggestions. This study was financed by the Coordenação de Aperfeiçoamento de Pessoal de Nível Superior—Brasil (CAPES)—Finance Code 001.

[1] F. Pretorius, Phys. Rev. Lett. **95**, 121101 (2005).

[2] M. Campanelli, C. O. Lousto, P. Maorroneti, and Zlochower, Phys. Rev. Lett. **96**, 111101 (2006).

[3] J. G. Baker, J. Centrella, D.-I. Choi, M. Koppitz, and J. van Meter, Phys. Rev. Lett. **96**, 111102 (2006).

[4] T. Nakamura, K. Oohara, and Y. Kojima, Prog. Theor. Phys. Suppl. **90**, 1 (1987).

[5] M. Shibata and T. Nakamura, Phys. Rev. D **52**, 5428 (1995).

[6] T. W. Baumgarte and S. L. Shapiro, Phys. Rev. D **59**, 024007 (1999).

[7] C. Bona, J. Massó, E. Seidel, and J. Stela, Phys. Rev. Lett. **75**, 600 (1995).

[8] M. Alcubierre, B. Brügmann, D. Pollney, E. Seidel, and R. Takahashi, Phys. Rev. D **64**, 061501 (2001).

[9] M. Alcubierre, B. Brügmann, P. Diener, M. Koppitz, D. Pollney, E. Seidel, and R. Takahashi, Phys. Rev. D **67**, 084023 (2003).

[10] J. D. Brown, Phys. Rev. D **79**, 104029 (2009).

[11] B. Brügmann, Int. J. Mod. Phys. D **08**, 85 (1999).

[12] P. Grandclément and J. Novak, Living Rev. Relativity **12**, 1 (2009).

[13] L. E. Kidder and L. S. Finn, Phys. Rev. D **62**, 084026 (2000).

[14] P. Grandclément, S. Bonazzola, E. Gourgoulhon, and J.-A. Mark, J. Comput. Phys. **170**, 231 (2001).

[15] M. Ansorg, B. Brügmann, and W. Tichy, Phys. Rev. D **70**, 064011 (2004).

[16] M. Ansorg, Classical Quantum Gravity **24**, S1 (2007).

[17] H. Pfeiffer, L. E. Kidder, M. A. Scheel, and S. A. Teukolsky, Comput. Phys. Commun. **152**, 253 (2003).

[18] P. C. M. Clemente and H. P. de Oliveira, Phys. Rev. D **96**, 024035 (2017).

[19] W. Barreto, P. C. M. Clemente, H. P. de Oliveira, and B. Rodriguez-Mueller, Phys. Rev. D **97**, 104035 (2018).

[20] L. E. Kidder, M. A. Scheel, S. A. Teukolsky, E. D. Carlson, and G. B. Cook, Phys. Rev. D **62**, 084032 (2000).

[21] M. A. Scheel, L. E. Kidder, L. Lindblom, H. P. Pfeiffer, and S. A. Teukolsky, Phys. Rev. D **66**, 124005 (2002).

[22] W. Tichy, Phys. Rev. D **74**, 084005 (2006); **80**, 104034 (2009).

[23] B. Szilágyi, L. Lindblom, and M. A. Scheel, Phys. Rev. D **80**, 124010 (2009).

[24] D. A. Hemberger, M. A. Scheel, L. E. Kidder, B. Szilágyi, G. Lovelace, N. W. Taylor, and S. A. Teukolsky, Classical Quantum Gravity **30**, 115001 (2013).

[25] S. Bonazzola, E. Gourgoulhon, P. Grandclément, and J. Novak, Phys. Rev. D **70**, 104007, 1 (2004).

[26] M. A. Scheel, H. P. Pfeiffer, L. Lindblom, L. E. Kidder, O. Rinne, and S. A. Teukolsky, Phys. Rev. D **74**, 104006 (2006).

[27] M. Alcubierre, Phys. Rev. D **55**, 5981 (1997).

[28] M. Alcubierre, Classical Quantum Gravity **20**, 607 (2003).

[29] T. W. Baumgarte and H. P. de Oliveira, Phys. Rev. D **105**, 064045 (2022).

[30] T. W. Baumgarte and D. Hilditch, Phys. Rev. D **106**, 044014 (2022).

[31] W. Heinrichs, Math. Comput. **53**, 103 (1989).

[32] W. Heinrichs, J. Sci. Comput. **6**, 1 (1991).

[33] J. P. Boyd, J. Comput. Phys. **143**, 283 (1998).

[34] J. P. Boyd, *Chebyshev and Fourier Spectral Methods* (Dover Publications, New York, 2001).

[35] M. A. Alcoforado, R. F. Aranha, W. Barreto, and H. P. de Oliveira, Classical Quantum Gravity **38**, 225004 (2021).

[36] M. A. Alcoforado, R. F. Aranha, W. Barreto, and H. P. de Oliveira, Phys. Rev. D **104**, 084065 (2021).

[37] W. Barreto, J. A. Crespo, H. P. de Oliveira, and E. L. Rodrigues, Classical Quantum Gravity **36**, 215011 (2019).

[38] M. A. Alcoforado, W. Barreto, and H. P. de Oliveira, Int. J. Mod. Phys. D **31**, 2250028 (2022).

[39] M. Alcubierre and M. D. Mendez, Gen. Relativ. Gravit. **43**, 2769 (2011).

[40] P. J. Montero and I. Cordero-Carrion, Phys. Rev. D **85**, 124037 (2012).

[41] T. W. Baumgarte, P. J. Montero, I. Cordero-Carrion, and E. Müler, Phys. Rev. D **87**, 044026 (2013).

[42] M. Alcubierre and B. Brügmann, Phys. Rev. D **63**, 104006 (2001).

[43] E. Jiménez-Vázquez and M. Alcubierre, Phys. Rev. D **105**, 064071 (2022).

[44] B. Brügmann, J. A, González, M. Hannam, S. Husa, and U. Sperhake, Phys. Rev. D **77**, 024027 (2008).

[45] T. W. Baumgarte and S. L. Shapiro, *Numerical Relativity* (Cambridge University Press, Cambridge, England, 2010).

[46] C. Canuto, A. Quarteroni, M. Y. Hussaini, and T. A. Zang, *Spectral Methods in Fluid Dynamics* (Springer-Verlag, Berlin, 1988).

[47] D. A. Kopriva, Appl. Numer. Math. **2**, 221 (1986); SIAM J. Sci. Stat. Comput. **10**, 120 (1989).

[48] M. Hannam, S. Husa, D. Pollney, B. Brügmann, and N. OMurchadha, Phys. Rev. Lett. **99**, 241102 (2007).

[49] M. Hannam, S. Husa, B. Brügmann, J. A. González, and U. Sperhake, J. Phys. Conf. Ser. **66**, 012047 (2007).

[50] J. R. Cash and A. H. Karp, ACM Trans. Math. Softw. **16**, 201 (1990).

[51] K. A. Dennison and T. W. Baumgarte, Classical Quantum Gravity **31**, 117001 (2014).

[52] T. W. Baumgarte and S. G. Naculich, Phys. Rev. D **75**, 067502 (2007).

[53] F. Estabrook, H. Wahlquist, S. Christensen, B. DeWitt, L. Smarr, and E. Tsiang, Phys. Rev. D **7**, 2814 (1973).

[54] J. S. Hesthaven and R. M. Kirby, Math. Comput. **77**, 1425 (2008).

[55] J. A. Faber, T. W. Baumgarte, Z. B. Etienne, S. L. Shapiro, and K. Taniguchi, Phys. Rev. D **76**, 104021 (2007).

[56] P. J. Montero, J. A. Font, and M. Shibata, Phys. Rev. D **78**, 064037 (2008).

[57] B. Brügmann, Gen. Relativ. Gravit. **41**, 2131 (2009).